

Synthesis of PtRu Nanoparticles from the Hydrosilylation Reaction and Application as Catalyst for Direct Methanol Fuel Cell

Junchao Huang,* Zhaolin Liu, Chaobin He, and Leong Ming Gan

Institute of Materials Research and Engineering (IMRE), 3 Research Link, Singapore 117602

Received: May 21, 2005; In Final Form: July 20, 2005

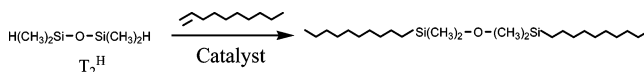
Nanosized Pt, PtRu, and Ru particles were prepared by a novel process, the hydrosilylation reaction. The hydrosilylation reaction is an effective method of preparation not only for Pt particles but also for other metal colloids, such as Ru. Vulcan XC-72 was selected as catalyst support for Pt, PtRu, and Ru colloids, and TEM investigations showed nanoscale particles and narrow size distribution for both supported and unsupported metals. All Pt and Pt-rich catalysts showed the X-ray diffraction pattern of a face-centered cubic (fcc) crystal structure, whereas the Ru and Ru-rich alloys were more typical of a hexagonal close-packed (hcp) structure. As evidenced by XPS, most Pt and Ru atoms in the nanoparticles were zerovalent, except a trace of oxidation-state metals. The electrooxidation of liquid methanol on these catalysts was investigated at room temperature by cyclic voltammetry and chronoamperometry. The results concluded that some alloy catalysts showed higher catalytic activities and better CO tolerance than the Pt-only catalyst; Pt₅₆Ru₄₄/C have displayed the best electrocatalytic performance among all carbon-supported catalysts.

Introduction

Metal and semiconductor nanoparticles have been extensively explored for many years due to their wide application in the fields of catalysis, photography, optics, electronics, optoelectronics, data storage, and biological and chemical sensor.^{1–6} Pt and Pt alloy nanoparticles are catalytically active in room temperature electrooxidation reactions of interest to direct methanol fuel cell (DMFC) applications. However, the performance of DMFC is significantly affected by CO concentrations in the fuel cell.⁷ This is because of the strong adsorption of carbon monoxide on the Pt anode, which inhibits the hydrogen oxidation reaction. It has been reported that electrocatalytic activities of the anode is significantly enhanced as Pt is alloyed with Ru, Sn, and Mo, etc. So far, the incorporation of Ru into the Pt catalyst has yielded the best results. To address the improved Pt catalytic activities toward methanol oxidation by Ru, two mechanisms have been proposed. One is the bifunctional mechanism: In the presence of Ru surface atoms, adsorbed CO is oxidized at potentials more negative than that on Pt. Thus, the Pt surface sites become more available for hydrogen adsorption and oxidation;⁸ the other mechanism is the ligand-effect mechanism: the modification of electronic properties of Pt via a Pt–Ru orbital overlap.⁹

It is well-known that the properties of metal nanoparticles, such as catalytic activity, photoluminance, and optical properties, are strongly dependent on the particle shape, size, and size distribution.^{10–16} Conventional preparation techniques based on wet impregnation and chemical reduction of the metal precursors often do not provide adequate control of particle shape and size.¹⁷ There are continuing efforts to develop alternative synthesis methods based on microemulsions,¹⁸ sonochemistry,^{19,20} microwave irradiation,^{21–25} and catalytic organic reaction,^{26,27} which are more conducive to generating nanoscale colloids or clusters with better uniformity.

SCHEME 1: Hydrosilylation Reaction



The hydrosilylation reaction, an addition of a hydrosilane unit (Si–H) to a double bond (C=C) to form an alkylsilane (Scheme 1), is widely utilized in the production of silicon polymers, liquid injection molding products, paper release coatings, and pressure-sensitive adhesives.²⁸ The hydrosilylation reaction can be initiated in numerous ways, and one of the most commonly used platinum-based catalysts is the Karstedt catalyst (platinum divinyltetramethyldisiloxane complex).^{29–31} During the course of the Pt-catalyzed hydrosilylation reaction, the formation of colloidal Pt species was previously regarded as an undesired side reaction, which resulted in coloration of the final reaction solution.³² In contrast, this “side reaction” can be exploited to synthesize Pt or Ru nanoparticles.

In the previous papers, we reported the synthesis of Pt nanoparticles from the hydrosilylation reaction,^{26,27} and microwave-assisted synthesis of carbon-supported PtRu nanoparticles,^{24,25,33,34} which could be applied as catalysts for direct methanol fuel cell. In the current paper, the electrooxidation of liquid methanol on Pt and PtRu alloy nanoparticles, synthesized from the hydrosilylation reaction, was investigated. Pt and Pt alloys show catalytic activities in room temperature electrooxidation reactions that are of interest to fuel cell applications. To the best of our knowledge, we are not aware of any other investigation into electrochemical properties of Pt and PtRu alloys synthesized in the hydrosilylation reaction. Moreover, we sought to extend this method to prepare other metal nanoparticles; it was found for the first time that Ru nanoparticles were successfully synthesized in the hydrosilylation reaction, and further studies on other metal nanoparticles are in progress.

* Corresponding author. Telephone: 65-68741972. Fax: 65-68727528. E-mail: jc-huang@imre.a-star.edu.sg.

TABLE 1: Formulation of the Hydrosilylation Reaction for Nanoparticle Synthesis

system	Ru(PPh ₃) ₃ Cl ₂	Pt(dvs) (10mM)	toluene (mL)	Reaction time (days)	Yield (%) ^a
Pt	0 mmol, 0 mg	0.041 mmol, 4.1 mL	14.0	2	96
Pt ₈₉ Ru ₁₁	0.01 mmol, 9.5 mg	0.0358 mmol, 3.58 mL	15.0	4	92
Pt ₇₇ Ru ₂₃	0.0198 mmol, 19.0 mg	0.0307 mmol, 3.07 mL	15.5	4	95
Pt ₅₆ Ru ₄₄	0.0395 mmol, 37.9 mg	0.0205 mmol, 2.05 mL	16.5	4	93
Pt ₂₆ Ru ₇₄	0.0593 mmol, 56.9 mg	0.0103 mmol, 1.03 mL	17.0	4	92
Ru	0.0792 mmol, 75.9 mg	0 mmol, 0 mL	18.0	5	90

^a The yield of the hydrosilylation reaction was calculated based on the amount of the metal starting materials.

Experimental Section

Chemicals. 1,1,3,3-Tetramethyldisiloxane (T₂^H) and dichlorotris(triphenylphosphine)ruthenium (Ru(PPh₃)₃Cl₂) were purchased from Aldrich and used as received. 1-Decene was purchased from Lancaster. Toluene was distilled over sodium/benzophenone under nitrogen immediately prior to use. Platinum divinyltetramethyldisiloxane complex (Pt(dvs)) was obtained from Aldrich and diluted to a 10 mM solution in anhydrous toluene before use. Other chemicals were used as received without further purification.

Synthesis of Pt, Ru, and PtRu Alloy Nanoparticles. T₂^H (2 mmol, 0.269 g), 1-decene (8 mmol, 1.124 g), and the predetermined amount (Table 1) of Ru(PPh₃)₃Cl₂ were placed in a 50 mL of Schlenk flask with a magnetic stirrer. The reaction flask was charged by anhydrous toluene and stirred at room temperature until all chemical dissolved in toluene. The flask was evacuated and refilled with nitrogen three times. After that, Pt(dvs) (10 mM solution) was added by a syringe, and then the reaction was stirred under nitrogen at 100 °C for several days. The reaction solutions were centrifuged; the black powders were obtained after decanting off the solvent. And, the samples were washed by toluene and centrifuged twice to remove the uncoordinated molecules and dried under vacuum. The formulation and yield of the hydrosilylation reaction were shown in Table 1. In the hydrosilylation reaction, two reaction catalysts, Pt(dvs) and Ru(PPh₃)₃Cl₂, were used, which induced the formation of Pt, PtRu, or Ru nanoparticles in reaction solutions. As the concentration of Pt(dvs) in the reaction solution increased, the reaction rate also increased, indicating catalytic activity of Pt(dvs) is higher than that of Ru(PPh₃)₃Cl₂.

Characterization. Transmission electron microscopy (TEM) images were acquired on a Philip CM300 TEM operating at an acceleration voltage of 300 kV. TEM samples were prepared by depositing several drops of diluted colloidal solution onto standard carbon-coated copper grids, followed by drying under ambient condition for 1 h. X-ray diffraction (XRD) patterns were recorded by a Bruker GADDS diffractometer with area detector using a Cu K α source ($\lambda = 0.1542$ nm) operating at 40 kV and 40 mA. XPS spectra were obtained using a VG Scientific Escalab 220 IXL with a monochromator Al K α X-ray source ($h\nu = 1486.6$ eV), and narrow scan photoelectron spectra were recorded for Ru 3p and Pt 4f. Fourier transform infrared (FTIR) spectra were measured with a Bio-Rad 165 FTIR spectrophotometer. ¹H NMR spectra were collected on a Bruker 400 spectrometer using chloroform-*d* as solvent and tetramethylsilane as internal standard. UV-vis spectra were collected using a SHIMADZU UV-2501PC UV-vis recording spectrophotometer.

Electrochemical Measurement. The Pt or PtRu nanoparticles were washed by toluene to get rid of uncoordinated molecules that formed in the hydrosilylation reaction. The Pt or PtRu nanoparticles were supported on high surface area Vulcan XC-72 carbon (20 wt % metal content) by combining a toluene dispersion of Pt nanoparticles with a suspension of Vulcan

carbon in toluene. The solution was vigorously stirred for 2 h. Solvent was evaporated and the powder was dried at 60 °C in a vacuum. To remove the stabilizing shell on the Pt nanoparticles, as-synthesized Pt/C catalysts were heat-treated in argon at 360 °C for 10 h. The furnace was purged with argon gas for at least 15 min prior to the heat treatment. The prepared Pt/C catalysts for electrochemical measurement had a nominal metal loading of 20 wt % on the Vulcan carbon black support.

An EG&G Model 273 potentiostat/galvanostat and a conventional three-electrode test cell were used for electrochemical measurements. The working electrode was a thin layer of Nafion-impregnated catalyst cast on a vitreous carbon disk held in a Teflon cylinder. The catalyst layer was prepared as reported previously.³³ Pt gauze and a saturated calomel electrode (SCE) were used as the counter and reference electrodes, respectively. All potentials quoted in this paper were referred to the SCE. All electrolyte solutions were deaerated by high-purity argon for 2 h prior to any measurement. For cyclic voltammetry and chronoamperometry of methanol oxidation, the electrolyte solution was 2 M CH₃OH in 1 M H₂SO₄, which was prepared from high-purity sulfuric acid, high-purity grade methanol, and distilled water.

Results and Discussion

Nanoparticles Preparation. In our previous paper,²⁷ when 1-decene and T₂^H were selected as starting materials, it was easy to prepare the carbon-supported Pt catalyst for the direct methanol fuel cell. Furthermore, when the hydrosilylation reaction was carried out at the excess olefin (1-decene) concentration, the byproducts containing the Si compound were easy to remove. Without a Si-contained shell, the catalytic activity of the PtRu nanoparticles was higher than those from other methods.

Inductively coupled plasma spectroscopy (ICP) was used to determine the actual platinum and ruthenium contents in PtRu alloy nanoparticles. The measured compositions of PtRu alloy nanoparticles were obtained as Pt₂₆Ru₇₄, Pt₅₆Ru₄₄, Pt₇₇Ru₂₃, and Pt₈₉Ru₁₁, where the numerical subscripts denote the weight percentage of the alloying metal. As compared to the theoretical compositions of Pt₂₅Ru₇₅, Pt₅₀Ru₅₀, Pt₇₅Ru₂₅, and Pt₈₇Ru₁₃, the measured ruthenium contents in the PtRu alloy nanoparticles were lower, likely due to the lower catalytic activity of Ru(PPh₃)₃Cl₂ in the hydrosilylation reaction.

Narrow-distributed Ru nanoparticles were successfully synthesized by the hydrosilylation reaction. Figures 1 and S1 (Supporting Information) present TEM images and high-resolution TEM (HRTEM) images of Ru nanoparticles from the hydrosilylation reaction. In the TEM images (Figure 1) Ru nanoparticles with a diameter of 3.5 nm were observed. Careful inspection (Figure S1 in Supporting Information) revealed that most Ru nanoparticles could be discernible as single crystals of hexagonal close-packed (hcp) lattice, because clear {101} lattice planes are observed to cover the whole particles if the particles were viewed in a proper direction. The lattice spacing,

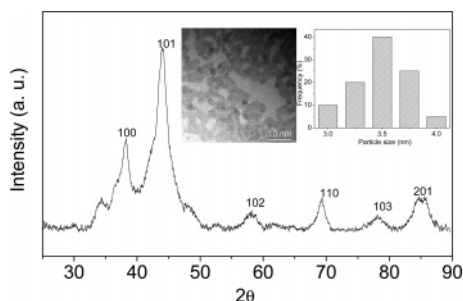


Figure 1. XRD pattern of Ru nanoparticles from the hydrosilylation reaction. Inserts show the TEM image and size distribution of Ru nanoparticles.

0.21 nm, is consistent with that of Ru metal³⁵ and the XRD results (Figure 1). The XRD patterns show several diffraction peaks that were indexed to {100}, {101}, {102}, {110}, {103}, {112}, and {201} planes of Ru, respectively. From the XRD patterns the mean particle sizes, 4.5 nm, were calculated by the Scherrer equation:³⁶

$$d (\text{\AA}) = \frac{k\lambda}{\beta \cos(\theta)}$$

where k is a coefficient (0.9), λ is the wavelength of X-ray used (1.540 56 \AA), β is the full width at half-maximum of the respective diffraction peak (rad), and θ is the angle at the position of the peak maximum (rad).

Morphology. The morphology of Pt nanoparticles from the hydrosilylation reaction has been fully characterized in our previous work.²⁷ In this paper, parts a and b of Figure 2 exhibit two typical TEM images of the as-synthesized nanoparticles Pt₈₉Ru₁₁ (Pt-rich alloy) and Pt₂₆Ru₇₄ (Ru-rich alloy); uniform and well-dispersed alloy particles were observed. As shown in Figure 2e,f, the average diameters of 2.4 (for Pt₈₉Ru₁₁) and 3.4 nm (for Pt₂₆Ru₇₄) were obtained by direct measurement of TEM images, as well as relatively narrow particle size distributions (± 0.4 nm). Careful investigation of TEM images (Figures S2 and S3 in the Supporting Information) revealed that clear lattice planes were observed to cover the whole particles if the particles are viewed in a proper direction; most PtRu nanoparticles could therefore be discernible as a single-crystal lattice, which indicated the formation of Pt-rich or Ru-rich alloys. All of the TEM images of other as-synthesized nanoparticles were shown in Figure S4 for reference (Supporting Information). Adsorption of the colloidal particles on Vulcan carbon followed by thermal treatment (in an argon gas at 360 °C for 10 h) to remove the stabilizing capping agents did not cause significant morphological changes (Figure 2c,d). The Pt and alloy nanoparticles were in a state of high dispersion over the carbon surface, and the size of the particles was nearly unchanged.

X-ray diffraction patterns provide a bulk analysis of the crystal structure, lattice constant, and crystal orientation of the as-synthesized PtRu nanoparticles and their supported catalysts for the fuel cell. Figure 3 shows the XRD pattern of the as-synthesized Pt, PtRu, and Ru nanoparticles. For Pt or Pt-rich alloy nanoparticles, several broad diffraction peaks could be indexed to the [111], [200], [220], and [311] planes of a Pt face-centered cubic (fcc) crystal structure. For Ru or Ru-rich alloy nanoparticles, the diffraction peaks could be indexed to the [100], [101], [110], [103], and [201] planes of a Ru hexagonal closed-packed (hcp) lattice. Similarly, the XRD patterns of the supported catalyst (Pt/C, PtRu/C, and Ru/C) were exhibited in Figure 4. The diffraction peaks in XRD patterns could be accordingly indexed to the planes of Pt (fcc) or Ru

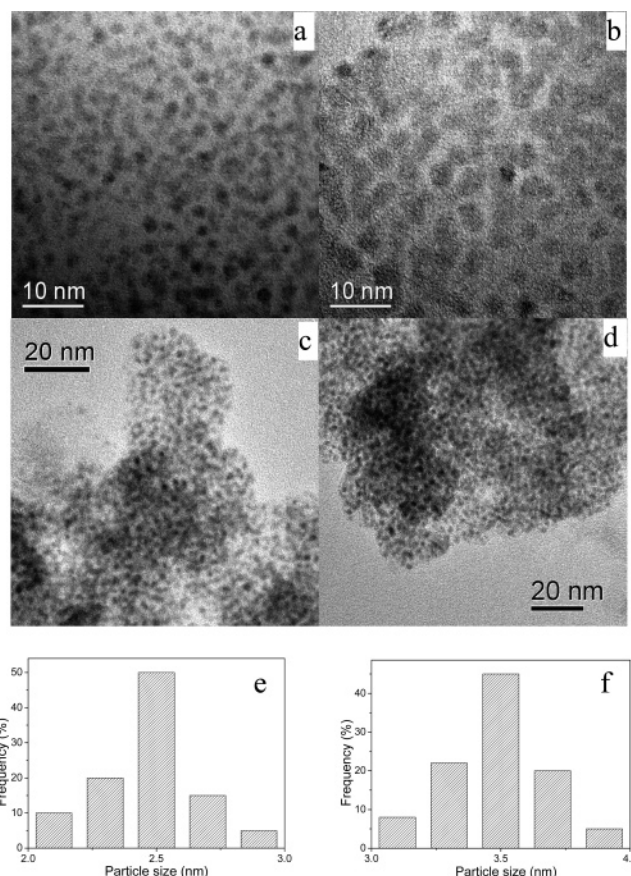


Figure 2. TEM images of the as-synthesized Pt₈₉Ru₁₁ (a) and Pt₂₆Ru₇₄ (b) colloids and the heat-treated Pt₈₉Ru₁₁/C (c) and Pt₂₆Ru₇₄/C (d) catalysts. Histograms of particle size distributions for the as-synthesized Pt₈₉Ru₁₁ (e) and Pt₂₆Ru₇₄ (f).

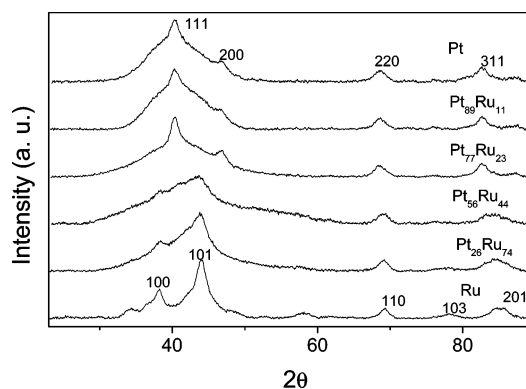


Figure 3. X-ray diffraction patterns of the as-synthesized Pt, PtRu, or Ru nanoparticles.

(hcp) lattices, respectively. It was also noted that after thermal treatment (in an argon gas at 360 °C for 10 h) the diffraction peaks increased in intensity and sharpness for Pt and Pt-rich alloy catalysts, an indication of increase in crystallinity of metals. The lattice constant of 3.924 \AA (for Pt/C catalysts) was in good agreement with 3.923 \AA for pure Pt. The strong diffraction at $2\theta < 35^\circ$ was observed in the Figure 4 due to the X-ray diffraction of the carbon black support.

As seen in the XRD patterns of the as-synthesized nanoparticles (Figure 3), usually Ru alone would display the feature reflections of a hcp lattice, and Pt would display the characteristic fcc reflections as described previously. The diffraction patterns of Pt-rich nanoparticles (Pt₇₇Ru₂₃ and Pt₈₉Ru₁₁) displayed mostly the reflection characteristics of the Pt fcc

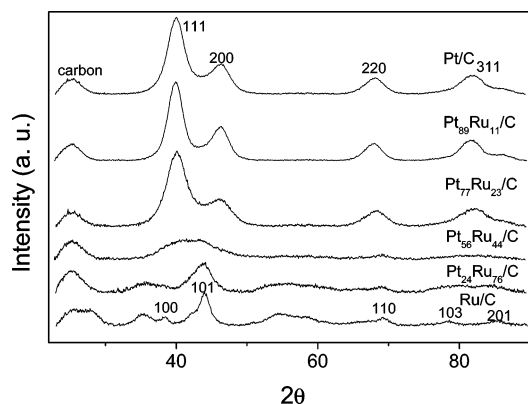


Figure 4. X-ray diffraction patterns of the heat-treated Pt/C, PtRu/C, or Ru/C catalysts for the fuel cell.

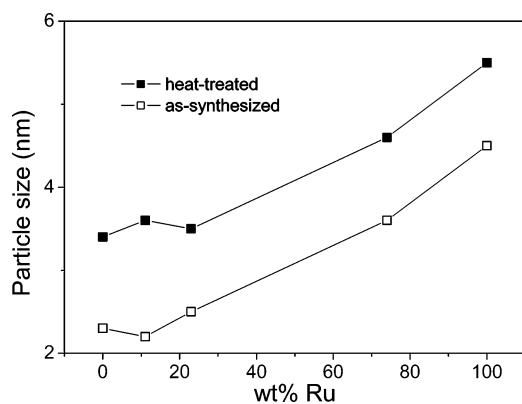


Figure 5. Dependence of particle size on Ru content of PtRu nanoparticles.

structure, indicating an alloy formation based on the substitution of the Pt lattice sites.³⁷ However, the hcp-featured pattern of Ru-rich alloy nanoparticles (Pt₂₆Ru₇₄) could be clearly identified, suggesting the formation of Ru-rich alloys. Likewise, the presence of Pt-rich or Ru-rich alloys was evidenced by the XRD patterns (Figure 4) of PtRu/C nanoparticles after heat treatment. The lattice structures observed in TEM images also agreed well with the XRD results.

The particle size in Figure 5 was a volume-average value calculated by the Scherrer equation. It was found that the as-synthesized and heat-treated Pt/C have particle sizes (<6 nm) of nanometer scale, which will lead to the heat-treated alloy nanoparticles of high catalytic activities in the application of fuel cell. Although there was a thermally induced limited particle growth observed in the heat treatment, the effect on catalytic activities of the alloy particles can be negligible. As seen in Figure 5, the size of both as-synthesized and heat-treated nanoparticles increases with increasing Ru concentration, from 2.3 to 4.5 nm for the as-synthesized samples and from 3.4 to 5.5 nm for the heat-treated samples. This trend of increasing particle size was also confirmed by TEM images (Figure S4 in Supporting Information). In addition, the particle size of Pt₅₆Ru₄₄ could not be calculated correctly from the Scherrer equation, because Pt-rich alloy and Ru-rich alloy possibly coexisted in this sample, and the diffraction peaks of both alloys were obscured by each other.

Careful investigation of Figure 4 reveals that all diffraction peaks were shifted synchronously to higher 2θ values with increasing Ru concentration in the Pt-rich alloys (Pt, Pt₈₉Ru₁₁, and Pt₇₇Ru₂₃). The shift was an indication of the reduction in lattice constant. The lattice constants (a_0) of Pt, Pt₈₉Ru₁₁, and Pt₇₇Ru₂₃ were 3.924, 3.908, and 3.895 Å, respectively. Accord-

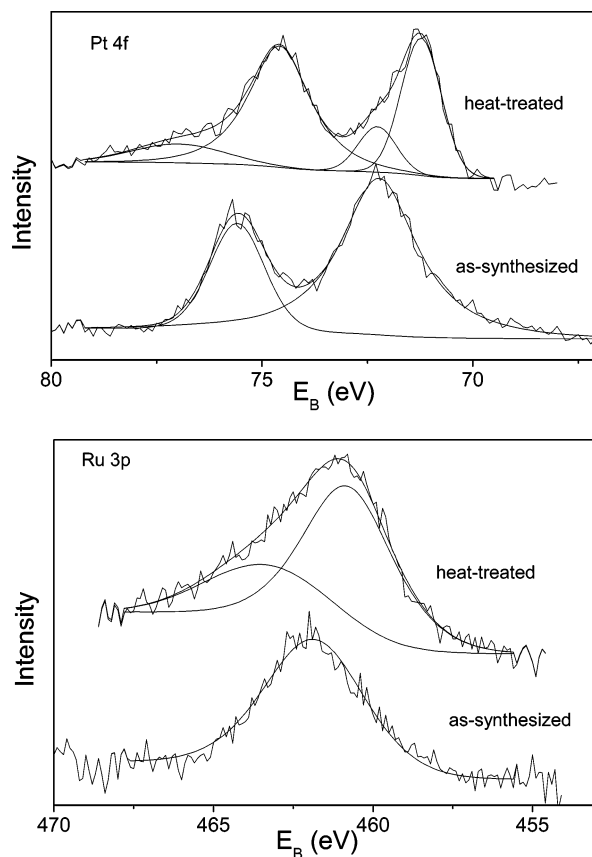


Figure 6. X-ray photoelectron spectra of the as-synthesized and heat-treated PtRu catalysts for fuel cell.

ing to Vegard's law, the lattice constant was usually used to measure the extent of alloying. The lattice constant for heat-treated Pt-rich alloy displayed a decrease monotonically with the Ru concentration. The reduction of lattice constant primarily arose from substitution of platinum atoms with Ru atoms, resulting in contraction of the fcc lattice, which indicated the formation of the PtRu alloy.

XPS. The surface oxidation states of the PtRu catalysts were investigated by X-ray photoelectron spectroscopy (XPS). Because the Ru3d binding energy (E_B) of zerovalent ruthenium at 284.3 eV³⁸ is very close to the C1s E_B resulting from adventitious carbonaceous species, the Ru3p line was used instead for the analysis of the Ru oxidation state. Figure 6 shows Pt4f, and Ru3p regions of the XPS spectrum of the as-synthesized, and heat-treated the Pt₅₆Ru₄₄/Vulcan carbon catalyst, respectively. After the thermal treatment (360 °C for 10 h), the slight shift in the Pt4f and Ru3d peaks to lower binding energy was likely caused by the removal of the capping agents on the nanoparticles and the change in the surface oxidation state. Before the thermal treatment of the PtRu catalyst, the Pt4f signal (Figure 6) could be deconvoluted into one pair of peaks at $E_B = 72.2$ and 75.6 eV, this could be assigned to the complex state of Pt-olefin, which was in good agreement with our previous results.²⁷ After the thermal treatment, the Pt4f signal consisted of two pairs of doublets. The most intense doublet (71.2 and 74.6 eV) was due to metallic Pt(0). The second set of doublets (72.3 and 76.3 eV) could be assigned to the Pt(II) chemical state.³⁹ Likewise, before the thermal treatment, the Ru3p_{3/2} signal of the PtRu nanoparticles could be convoluted into one peak at $E_B = 461.9$ eV, and after the thermal treatment, the Ru3p_{3/2} signal could be deconvoluted into two distinguishable peaks of different intensities at $E_B = 461.0$ and 462.9 eV, which corresponded well with Ru(0) and RuO₂,⁴⁰ respectively. It was

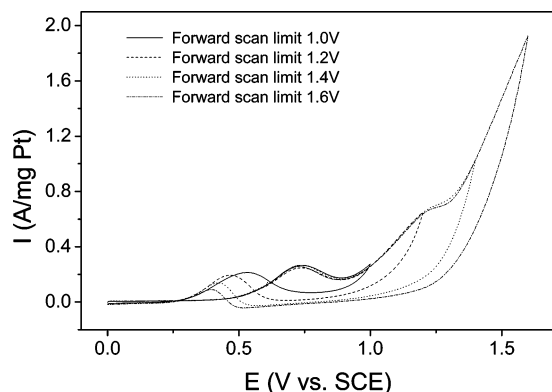


Figure 7. Cyclic voltammograms of room-temperature methanol oxidation on the heat-treated Pt/C catalysts in 1 M H₂SO₄ and 2 M CH₃OH at 50 mV/s for different potential scan limits.

also noted that the slight shift of the Ru_{3p_{3/2}} binding energy was likely attributed to the removal of the capping agent on the alloy nanoparticles.

Electrochemical Performances. In the previous experiments,³³ both the as-synthesized and heat-treated Pt/C catalysts were characterized by cyclic voltammetry (0–1 V, 50 mV/s) in an electrolyte of 1 M H₂SO₄ and 2 M CH₃OH; the as-synthesized Pt/C catalyst displayed an almost featureless voltammogram with low current density values, indicating the poor catalytic activities in methanol electrooxidation. Therefore, in this report all electrical measurements were carried out on the heat-treated catalyst (Pt/C or PtRu/C at 360 °C for 10 h).

The voltammograms of methanol oxidation on all heat-treated Pt/C catalysts consisted of two parts, i.e., the forward scan and the reverse scan. In the forward scan, methanol oxidation produced a prominent symmetric anodic peak around 0.65 V. In the reverse scan, an anodic peak current density was detected at around 0.44 V. Manohara and Goodenough attributed this anodic peak in the reverse scan to the removal of the incompletely oxidized carbonaceous species formed in the forward scan.⁴¹ These carbonaceous species are mostly in the form of linearly bonded Pt=C=O, the accumulation of intermediate carbonaceous species on the catalysts surface leading to “catalyst poisoning”. Hence the ratio of the forward anodic peak current density (I_f) to the reverse anodic peak current density (I_b), I_f/I_b , can be used to describe the catalyst tolerance to carbonaceous species accumulation. Low I_f/I_b ratio indicates poor oxidation of methanol to carbon dioxide during the anodic scan and excessive accumulation of carbonaceous residues on the catalyst surface. High I_f/I_b ratio shows the converse case.

The effect of the potential scan limit on the backward scan current is shown in Figure 7. Since the backward scan peak current decreased with increasing the anodic limit in the forward scan, it appeared that the backward scan peak was primarily associated with residual carbon species on the surface rather than the oxidation of freshly chemisorbed species. The reaction of the backward scan peak as mentioned by Manohara and Goodenough⁴¹ would be written as $\text{PtOH}_{\text{ad}} + \text{Pt}=\text{C}=\text{O} \rightarrow \text{CO}_2 + 2\text{Pt} + \text{H}^+ + \text{e}^-$, so the I_f/I_b ratio increased with the anodic limit.

As shown in Table 2, the catalytic performance of the heat-treated Pt/C (10 h) and PtRu/C (10 h) catalysts with different Ru contents was analyzed and compared in the following attributes: the onset potential of methanol oxidation (the potential where $I \geq 0.025$ A/(mg of Pt)), the anodic peak potential, the ratio of the forward anodic peak current density (I_f) to the reverse anodic peak (I_b), and chronoamperometry.

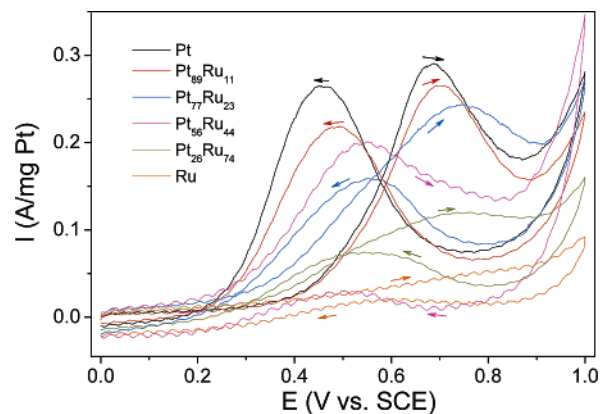


Figure 8. Cyclic voltammograms of room-temperature methanol oxidation on the heat-treated Pt/C and PtRu/C catalysts in 1 M H₂SO₄ and 2 M CH₃OH at 50 mV/s.

TABLE 2: Performance of the Heat-treated Pt/C and PtRu/C Catalysts

catalyst	potentials		
	onset	anodic peak	I_f/I_b ratio
Pt/C	0.40	0.69	1.10
Pt ₈₉ Ru ₁₁ /C	0.39	0.70	1.21
Pt ₇₇ Ru ₂₃ /C	0.28	0.74	1.54
Pt ₅₆ Ru ₄₄ /C	0.20	0.55	6.73
Pt ₂₆ Ru ₇₄ /C	0.36	0.71	1.60
Ru/C	0.48		

As seen from Figure 8, there was no significant feature difference between the voltammograms of carbon-supported Pt catalyst and carbon-supported PtRu alloy catalysts. Anodic peaks appeared in both the forward and reverse scans. The forward anodic peak current density of methanol oxidation over heat-treated Pt/C and PtRu/C catalysts decreased in the order Pt > Pt₈₉Ru₁₁ > Pt₇₇Ru₂₃ > Pt₅₆Ru₄₄ > Pt₂₆Ru₇₄. This was understandable, as alloying by Ru would cause a dilution of the platinum concentration on the catalyst surface. Comparing with the voltammograms of other Pt/C or PtRu/C catalysts, it was noticeable that the forward anodic peak of the catalyst Pt₅₆Ru₄₄/C was observed to shift cathodically to 0.55 V, this would likely arise from its exceptional heat-treated crystalline structure as shown in its XRD pattern (Figure 4).

In accordance with Goodenough’s report, the anodic peak in the backward scan, which indicates the removal of carbonaceous species not completely oxidized in the anodic scan,⁴¹ the ratio of I_f/I_b can be used as an indicator of the catalyst tolerance to carbonaceous species. The heat-treated Pt/C catalyst had the lowest I_f/I_b ratio of 1.10 (Table 2), confirming the known low CO tolerance of Pt catalysts. The catalyst, Pt₅₆Ru₄₄/C, presented the anodic current density ratio of 6.73, suggesting the least carbonaceous accumulation and the most “tolerance” toward CO poisoning. This could be attributed to the presence of Pt–Ru pair sites on the catalysts surface, and Ru is known to adsorb carbonaceous species more favorably than pure Pt. However, in Ru-rich catalyst (Pt₂₆Ru₇₄/C), the electrochemical activity became virtually inactive mainly because ruthenium played a role in the dissociation of carbonaceous species, not in the promotion of the methanol oxidation reaction.

Table 2 shows that comparison between the different carbon-supported catalysts, the onset potential for heat-treated Pt/C was detected at 0.40 V, when the weight percent of ruthenium increased to 44%, i.e., heat-treated Pt₅₆Ru₄₄/C; the onset potential was lowered to 0.21 V. However, the weight percent of ruthenium continuously increased to 75%; the onset potential shifted up to 0.36V.

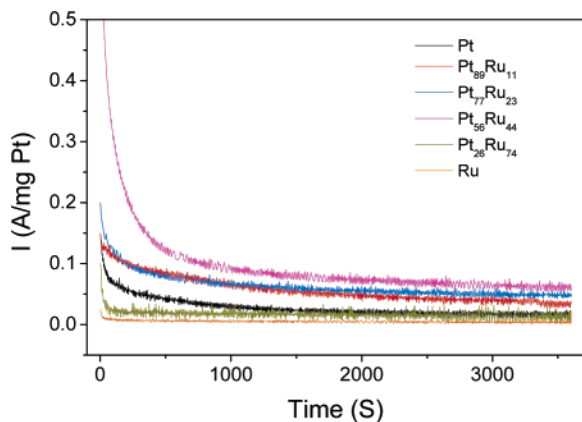


Figure 9. Polarization current vs time plots for the room-temperature electrooxidation of methanol on the heat-treated Pt and PtRu catalysts in 1 M H₂SO₄ and 2 M CH₃OH electrolyte at 0.4 V (vs SCE).

Figure 9 shows the different curves of current decay for each carbon-supported catalyst. For heat-treated Pt/C and Pt₉₉Ru₁₁, the rate of current decay was higher than others even after 1 h, supposedly because of catalyst poisoning by the chemisorbed carbonaceous species. The heat-treated Pt₅₆Ru₄₄/C was able to maintain the highest current density and the low rate of current decay for over 1 h among all the catalysts. The catalytic activity of Pt₂₆Ru₇₄ catalysts was worse than that of pure Pt, as a result of ruthenium dissolution over long electrochemistry time. In conclusion, the Pt₅₆Ru₄₄/C catalyst displayed the best electrocatalytic performance among all carbon-supported Pt-based catalysts prepared in this paper.

Conclusion

Pt and PtRu nanoparticles supported on Vulcan XC-72 carbon were prepared by a unique approach, the hydrosilylation reaction. Pt and its alloy particles were nanoscopic-sized and had narrow particle size distributions. XRD analysis revealed that the as-synthesized nanoparticles already had considerable crystallinity, as well as the heat-treated nanoparticles. All Pt-rich catalysts displayed the characteristic diffraction peaks of the Pt fcc structure, but the 2θ values were all shifted to slightly higher values, while the Ru-rich catalysts displayed the feature peaks of the Ru hcp structure. XPS results showed that the catalysts mainly composed of Pt(0) and Ru(0), with traces of oxidation states Pt and Ru. The Pt and PtRu catalysts, especially the bimetallic system of Pt₅₆Ru₄₄, showed excellent catalytic activities in room-temperature electrooxidation of methanol. Some alloy catalysts were more active than the Pt-only catalyst and more tolerant toward CO poisoning, as expected from the bifunctional mechanism of alloy catalysts.

Supporting Information Available: High-resolution TEM images of Ru and PtRu alloy nanoparticles and TEM images of the as-synthesized Pt, PtRu, and Ru nanoparticles. This material is available free of charge via the Internet at <http://pubs.acs.org>.

References and Notes

- Sun, Y.; Xia, Y. N. *J. Am. Chem. Soc.* **2004**, *126*, 3892.
- Zamborini, F. P.; Gross, S. M.; Murray, R. W. *Langmuir* **2001**, *17*, 481.
- Ye, H.; Scott, R. W. J.; Crooks, R. M. *Langmuir* **2004**, *20*, 2915.
- Yee, C.; Scotti, M.; Ulman, A.; White, H.; Tafailovich, M.; Sokolov, J. *Langmuir* **1999**, *15*, 4314.
- Hasan, M.; Bethell, D.; Brust, M. *J. Am. Chem. Soc.* **2002**, *124*, 1132.
- Rautaray, D.; Kumar, P. S.; Wadgaonkar, P. P.; Sastry, M. *Chem. Mater.* **2004**, *16*, 988.
- Lemons, R. A. *J. Power Sources* **1990**, *29*, 251.
- Gasteiger, H. A.; Markovic, N.; Ross, P. N.; Cairns, E. J. *J. Phys. Chem.* **1994**, *98*, 617.
- Frelink, T.; Visscher, W.; Van Veen, J. A. R. *Langmuir* **1996**, *12*, 3702.
- Link, S.; Beeby, A.; FitzGerald, S.; El-Sayed, M. A.; Schaaff, T. G.; Whetten, R. L. *J. Phys. Chem. B* **2002**, *106*, 3410.
- Woehle, G. H.; Warner, M. G.; Hutchison, J. E. *J. Phys. Chem. B* **2002**, *106*, 9979.
- Yang, Y.; Chen, S. *Nano Lett.* **2003**, *3*, 75.
- Negishi, Y.; Tsukuda, T. *J. Am. Chem. Soc.* **2003**, *125*, 4063.
- Wilcoxon, J. P.; Provencio, P. *J. Phys. Chem. B* **2003**, *107*, 12949.
- Buining, P. A.; Humbel, B. M.; Philipse, A. P.; Verkleij, A. J. *Langmuir* **1997**, *13*, 3921.
- Liu, S. M.; Gan, L. M.; Liu, L. H.; Zhang, W. D.; Zeng, H. C. *Chem. Mater.* **2002**, *14*, 1391.
- Armadi, I. S.; Wang, Z. L.; Green, T. C.; Henglein, A.; El-Sayed, M. A. *Science* **1996**, *272*, 1924.
- Liu, Z. L.; Lee, J. Y.; Han, M.; Chen, W. X.; Gan, L. M. *J. Mater. Chem.* **2002**, *12*, 2453.
- Okitsu, K.; Yue, A.; Tanabe, S.; Matsumoto, H. *Chem. Mater.* **2000**, *12*, 3006.
- Fujimoto, T.; Terauchi, S.; Umehara, H.; Kojima, I.; Henderson, W. *Chem. Mater.* **2001**, *13*, 1057.
- Yu, W. Y.; Tu, W. X.; Liu, H. F. *Langmuir* **1999**, *15*, 6.
- Tu, W. X.; Liu, H. F. *Chem. Mater.* **2000**, *12*, 564.
- Komarneni, S.; Li, D. S.; Newalkar, B.; Katsuki, H.; Bhalla, A. S. *Langmuir* **2002**, *18*, 5959.
- Chen, W. X.; Lee, J. Y.; Liu, Z. L. *Chem. Commun.* **2002**, 2588.
- Liu, Z. L.; Lee, J. Y.; Chen, W. X.; Han, M.; Gan, L. M. *Langmuir* **2004**, *20*, 181.
- Huang, J.; He, C.; Liu, X.; Xiao, Y.; Mya, K. Y.; Chai, J. *Langmuir* **2004**, *20*, 5145.
- Huang, J.; Liu, Z.; Liu, X.; He, C.; Chow, S. Y.; Pan, J. *Langmuir* **2005**, *21*, 699.
- Lewis, L. N.; Stein, J.; Gao, Y.; Colborn, R. E.; Hutchins, G. *Platinum Met. Rev.* **1997**, *41*, 66.
- Hichcock, P. B.; Lappert, M. F.; Warhurst, N. J. W. *Angew. Chem., Int. Ed. Engl.* **1991**, *30*, 438.
- Zhang, C.; Laine, R. M. *J. Am. Chem. Soc.* **2000**, *122*, 6979.
- Huang, J. C.; Li, X.; Lin, T.; He, C.; Mya, K. Y.; Xiao, Y.; Li, J. *J. Polym. Sci., Part B: Polym. Phys.* **2004**, *42*, 1173.
- Marko, I. E.; Sterin, S.; Buisini, L.; Mignani, G.; Branlard, P.; Tinant, B.; Declercq, J. *Science* **2002**, *298*, 204.
- Liu, Z.; Ling, X. Y.; Su, X.; Lee, J. Y. *J. Phys. Chem. B* **2004**, *108*, 8234.
- Liu, Z.; Lin, X.; Lee, J. Y.; Zhang, W.; Han, M.; Gan, L. M. *Langmuir* **2002**, *18*, 4054.
- The International Centre for Diffraction Data JCPDS-ICDD, PDF-2 Data Base. <http://www.icdd.com>.
- Warren, B. E. In *X-ray Diffraction*; Addison-Wesley: Reading, MA, 1996.
- Antolini, E.; Giorgi, L.; Cardellini, F.; Passalacqua, E. *J. Solid State Electrochem.* **2001**, *5*, 131.
- Moulder, J. F.; Stickle, W. F.; Sobol, P. E.; Bomben, K. D. In *Handbook of X-ray Photoelectron Spectroscopy*; Perkin-Elmer: Eden Prairie, MN, 1992.
- Woods, R. *J. Electroanal. Chem.* **1976**, *9*, 1.
- Wagner, C. D.; Riggs, W. M.; Davis, L. E.; Moulder, J. F. In *Handbook of X-ray Photoelectron Spectroscopy*; Mullemberg, G. E., Ed.; Perkin-Elmer: Eden Prairie, MN, 1978.
- Manohara, R.; Goodenough, J. B. *J. Mater. Chem.* **1992**, *2*, 875.